# Fabrication of high aspect ratio AlN nanopillars by top-down approach combining plasma etching and wet etching

Lucas Jaloustre, Saron Sales de Mello, Sébastien Labau, Camille Petit-Etienne, Erwine Pargon

▶ **To cite this version:**

Lucas Jaloustre, Saron Sales de Mello, Sébastien Labau, Camille Petit-Etienne, Erwine Pargon. Fabrication of high aspect ratio AlN nanopillars by top-down approach combining plasma etching and wet etching. Materials Science in Semiconductor Processing, 2024, 181, pp.108615. 10.1016/j.mssp.2024.108615 . hal-04625933

**HAL Id: hal-04625933**

**https://hal.univ-grenoble-alpes.fr/hal-04625933v1**

Submitted on 9 Oct 2024

**HAL** is a multi-disciplinary open access archive for the deposit and dissemination of scientific research documents, whether they are published or not. The documents may come from teaching and research institutions in France or abroad, or from public or private research centers.

L'archive ouverte pluridisciplinaire **HAL**, est destinée au dépôt et à la diffusion de documents scientifiques de niveau recherche, publiés ou non, émanant des établissements d'enseignement et de recherche français ou étrangers, des laboratoires publics ou privés.

# Fabrication of high aspect ratio AlN nanopillars by top-down approach combining plasma etching and wet etching

Jaloustre Lucas [a], Sales De Mello Saron [a], Labau Sébastien [a], Petit-Etienne Camille [a], Pargon Erwine [a*]

[a] *Univ. Grenoble Alpes, CNRS, CEA/LETI-Minatec, Grenoble INP, Institute of Engineering and Management University Grenoble Alpes, LTM, Grenoble F-38054, France*

* erwine.pargon@cea.fr, *Univ. Grenoble Alpes, CNRS, LTM, 17 rue des Martyrs, 38054 Cedex 09 Grenoble, France*

## Abstract

This study proposes a top-down approach for fabricating high aspect ratio AlN pillars with *m*-oriented nonpolar sidewalls, which will serve as the first building block for the fabrication of core-shell UV-LEDs. Such structures are achieved through a two-step process, combining a chlorine plasma etching, followed by a wet chemical etching with KOH. In this work, the mechanisms driving the AlN etching in chlorine plasma are discussed. In particular, we highlight the impact of the ratio between ion flux and radical flux on AlN etch rates, pillar profiles, and crystal orientation-dependent etching. We also identify two mechanisms of passivation layer formation on the pillar sidewalls that contribute to the pattern slope: redeposition of the carrier wafer etch by-products and Aluminium line of sight redeposition, both phenomena are also driven by the ionic bombardment. Low ionic bombardment (either low ion over radical flux ratio or low ion energy) has been identified as plasma conditions allowing the patterning of anisotropic AlN pillars but with the formation of *a*-nonpolar facets. Due to the inability to obtain *m*-oriented sidewalls using $Cl_2$ plasma etching alone, we show that the use of a KOH wet etching treatment allows verticalizing the pillars and revealing smooth *m*-facets on the pillars' sidewalls if suitable *m*-oriented hard mask is used. In this wet etching step, we highlight the key role played by the hard mask and its initial shape during the wet etching if straight and *m*-oriented pillars are desired.

**Keywords:** AlN, Plasma etching, KOH wet etching, preferential crystallographic etching.

## 1. Introduction

III-nitride (III-N) semiconductor light-emitting diodes (LEDs) are a particularly promising alternative to mercury vapor lamps for making compact, environmentally friendly, low-power UV sources [1]. The most classical approach today to emit in the UV-C range (λ=280-200 nm) is the growth of Al-rich (>50%) AlGaN quantum wells in AlN barrier on AlN *c*-crystalline plane [2].

However, the external quantum efficiency (EQE) of current planar AlGaN well-based UV LEDs is extremely low, of a few percent, compared to that of current blue LEDs (EQE~ 90%) [3].

Three-dimensional (3D) core−shell architecture offers some promising solutions to increase the EQE [4–6]. It uses micro/nanowires as a core template on which the emissive QWs are grown radially. This 3D geometry provides some advantages over the planar architecture: 1) reduced crystalline defects in the emissive layer [7,8]; 2) mitigation of the Quantum Stark Effect through growth on nonpolar *m*-planes where strong spontaneous and piezoelectric polarization are absent, compared to *c*-planes [9], 3) increased emissive surface area [10], and 4) enhanced light extraction [10].

To reach UV-C emission, the core-shell architecture involves the fabrication of well-organized arrays of AlN nanowires upon which the emissive $Al_{>50\%}GaN$ quantum wells (the shell) are radially grown. Ideally, the pillars should present a high aspect ratio (AR) with sub-micrometric diameter and several microns height. First, because the emitting active area is proportional to 4 times the aspect ratio [6]. Secondly, because sub-micrometer diameter pillar allows stress relaxation during QW growth and limits crack formation [11].

Unfortunately, in contrast to other III-V or III-N materials, the fabrication of AlN nanowires by bottom-up approaches, either by Molecular Beam Epitaxy (MBE) [12] or selective area growth via metal-organic vapor phase epitaxy (MOVPE) [13] remains immature.

Thus, the top-down approach, which combines lithography and plasma etching steps, shows significant promise for patterning arrays of high AR AlN nanopillars with controlled shapes, dimensions, and densities on a wafer-scale, as a core template for the AlGaN-based QW growth. However, to obtain a high quality of the QW regrowth on the core, the nanopillars should present smooth and *m*-oriented nonpolar facets on their sidewalls. Unfortunately, one challenge associated with the plasma patterning of deep etching of III-N layer is the potential for generating damaged and rough surfaces on the sidewalls, which may prevent high-quality surface regrowth [14].

The patterning of high aspect ratio AlN patterns is far more complicated than for other III-N. Chlorine-based plasma chemistries ($Cl_2$, $BCl_3$, $SiCl_4$) are typically used to etch AlN since they allow the formation of volatile products such as $AlCl_3$, $N_2$, and eventually $NCl_3$ [15–23]. However, under the same plasma conditions, AlN etch rates are 3 to 4 times lower than other III-N ones [20–23] This introduces etch selectivity issues with the etching mask if deep etching (>1µm) is targeted. The majority of studies devoted to the etching of AlN patterns are limited to sub-micron etched depths [17–19]. They all show AlN patterns with tapered profiles (slope of 70-80°) and rough sidewalls, highlighting the complexity of structuring this material.

To address the etch selectivity issue for AlN deep etching (>1µm), metallic hard masks obtained by lift-off

lithography are generally used but they can be a source of metallic contamination and pattern sidewalls roughness [16]. However, one group [15], reported on the nanofabrication of high-quality AlN nanorod arrays using a metallic mask. The metal dot mask was achieved by a lift-off process using Displacement Talbot and the plasma transfer used an $Ar/Cl_2$ plasma. Their best process allowed the patterning of highly anisotropic AlN nanorods, an AlN etch rate of 123 nm/min and an etch selectivity over the Ni hard mask of 31 [15]. However, despite the excellent etch selectivity, AlN pattern profile degradation started to appear for etching deeper than 2 µm, because of the Ni mask faceting and shrinkage, limiting the fabrication of nanorods with an aspect ratio to about 5-6. In subsequent studies [24,25], they used additional KOH-based wet etching to remove the plasma damage and tune the morphology and the diameter of the nanorods. Their two-step dry-wet etching process allows the fabrication of highly anisotropic nanorods with smooth sidewalls, a diameter of about 130 nm, and a height of 1.8 µm.

This article aim to provide a fabrication process flow to pattern high aspect ratio (>10, etch depth of 4 µm) AlN pillar arrays with smooth *m*-oriented facets that could be used for deep UV core/shell LEDs.

The first part of the experimental results section is dedicated to the plasma etching mechanisms involved in the $Cl_2$ plasma patterning of AlN pillars with a $SiO_2$ dielectric mask. The second part focuses on a post-plasma treatment using wet etching of AlN in 44% KOH solution at room temperature. The third experimental part draws a comparison between the etching mechanisms in $Cl_2$ plasma and wet KOH. Finally, we demonstrate that by combining an *m*-oriented hexagonal hard mask shape with optimized plasma and wet process conditions, homogeneous arrays of high aspect ratio AlN nanowires presenting anisotropic and smooth m-oriented sidewalls in a various range of dimensions and densities can be obtained.

## 2. Experimental setup

### 2.1. Sample preparation

Micro-pillar fabrication was carried out on a commercially available 2-inch wafer of unintentionally doped Al-polar (0001) AlN of 4 µm thickness grown on a *c*-sapphire substrate and provided by Nanowin company. A 1400 nm thick $SiO_2$ hard mask (HM) was deposited onto the AlN layer using Plasma Enhanced Chemical Vapor Deposition (PECVD) with tetraethoxysilane (TEOS) at 480 °C in a DxZ CVD reactor from Applied Materials. The 2-inch wafer is then diced into samples of 7 by 11 mm.

An electron-sensitive resist (ma-N 2410, with a thickness of 800 nm) is then spin-coated on the samples. The resist is then patterned using electron beam lithography (e-beam). The patterns consist of dots with hexagonal shapes and diameters (inscribed circles) of 0.25 µm, 0.35 µm, 0.5 µm, 1 µm, and 2 µm. The hexagonal dots had two orientations corresponding to *a*-planes {11-2k} and *m*-planes {10-1k} of AlN, with a precision of ±1° (cf. Fig. 1-a). The dots follow a staggered arrangement with three different densities: a dense array with a distance between the dots of 2 µm, a semi-dense array with a distance between the dots of 5 µm, and an isolated array with a distance between the dots of 15 µm (cf. Fig. 1-b). The primary focus of this work will be on the 0.5 µm diameter pillars within the semi-dense array, but the observed trends are consistent across different pitches and diameters.

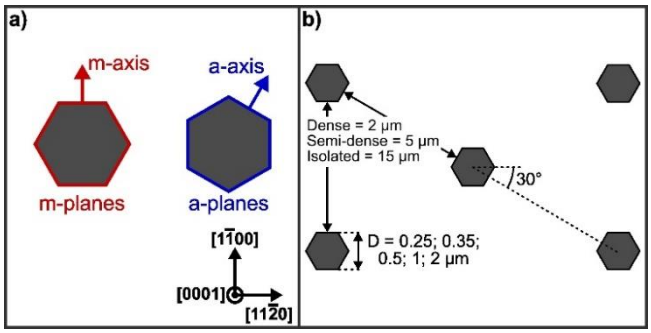


*Figure 1. a) Schematic of the shapes of the lithography dots, hexagonal oriented with a- or m-planes of the AlN or circular. b) Staggered arrangement of the dots with the annotations of dots diameters and distance between dots for the two arrays.*

### 2.2. Plasma and wet processes

The etching experiments were conducted using a Centura 5200 etch platform from Applied Materials, which consists of three plasma reactors designed for 200 mm wafers. For the HM opening step, the AlN sample is glued on a Si carrier wafer with a thermal paste and the process uses an $Ar/C_4F_8/O_2$ plasma in a Magnetically Enhanced Reactive Ion Etching (MERIE). Subsequently, for both resist stripping, and AlN etching steps, the sample is glued on a $Si_3N_4$ CW. Both processes were carried out in an Inductively Coupled Plasma (ICP) reactor (Decoupled Plasma Source, DPS). The resist was stripped using an $O_2$ plasma while the AlN layer was etched with a $Cl_2$ plasma.

The starting point for the AlN plasma process development was a recipe given the best patterning of high aspect ratio GaN pillars [26]: a gas flow of 190 sccm of $Cl_2$, a source power of 400 W, a bias power of 150 W (equivalent to a direct current self-bias voltage, $V_{DC}$, of -460 V), a pressure of 20 mTorr, with a chuck temperature maintain at 55 °C.

In this study, we investigated the impact of pressure, source power, and bias power while keeping fixed gas flow, $V_{DC}$ (except for bias power experiments), and wafer temperature, as detailed in Table 1. In a plasma, the $V_{DC}$ is directly correlated with the ion energy: $E_{ion} = |V_{DC}| + V_P$, (where $V_P$ is the plasma potential which is generally of about 10 to 15 eV and changes only of few eV with pressure, but not with the other parameters [27]). The main physical parameters that drive a plasma process are the radical flux (here the atomic chlorine flux $\Gamma_{Cl}$), and the ionic bombardment that combines the action of the ion flux ($\Gamma_i$) and the ion energy ($E_{ion}$) [28]. In our tool, the $V_{DC}$ (~ $E_{ion}$) is not an adjustable parameter but

rather a read-only value. To modify the ion energy, the accessible tool knob is the bias power, which is proportional to the product of the ion flux ($\Gamma_i$) (equivalent to a current/cm$^2$) and the $V_{DC}$ (~$E_{ion}$) [29]. When changing the source power or the pressure, the ion flux ($\Gamma_i$) is modified. This means that the bias power needs to be adjusted to guarantee a constant ion energy when the pressure or source power is varied. In our experiments, we adjust the bias power to keep a constant $V_{DC}$ (~$E_{ion}$) at about -460V, except for the bias power experiments.

*Table1. Experiment number, pressure, source power, bias power, corresponding DC bias, and time use to etch the AlN pillars.*

| Exp. n° | Pressure (mTorr) | Source power (W) | Bias power (W) | DC bias (V) | Etching time (s) |
|---|---|---|---|---|---|
| 1 | 10 | 400 | 220 | -460 | 1150 |
| 2 | 15 | 400 | 175 | -464 | 1650 |
| 3 | 20 | 400 | 150 | -454 | 2250 |
| 4 | 30 | 400 | 150 | -466 | 3420 |
| 5 | 20 | 400 | 80 | -338 | 4250 |
| 6 | 20 | 400 | 200 | -526 | 1780 |
| 7 | 20 | 200 | 150 | -465 | 2950 |
| 8 | 20 | 800 | 210 | -460 | 1200 |

The wet etching experiments were performed in a chemical fume hood located within a clean room, with the temperature maintained at 20 °C. To remove the $SiO_2$ hard mask after AlN etching, a commercial fluorhydric acid (HF) solution provided by TECHNIC consisting of 50 wt% HF diluted in water was employed for a 5-minute duration. In some cases, it could be important to keep the HM present to ensure complete removal of the sidewall passivation formed after plasma etching. For this purpose, a 1 wt% HF solution diluted in water was used for 60 seconds. Subsequently, a 44 wt% KOH solution provided by CMC Materials was used at room temperature for the post-etching wet treatment. Following the wet treatments, the samples were rinsed in deionized water for 2 minutes and dried using a nitrogen ($N_2$) flow. Various KOH etching times were investigated, ranging from 20 seconds to 2 hours, only the most noteworthy will be discussed.

All the details regarding the fabrication process, including resist, spin-coating, and e-beam parameters, as well as information about sample cleaning steps, are provided in our previous works [26,30].

### 2.3. Morphological characterizations

A FEI Helios-450s Focused Ion Beam Scanning Transmission Electron Microscopy (FIB-STEM) system was used to image the pillars after the different steps of dry and wet etching and to prepare Transmission Electron Microscopy (TEM) lamella. Observations were performed at 3 kV and 50 pA to minimize charging effects, and the samples were tilted by 45 ° to show the sidewalls of the pillars.

Before the TEM lamella preparation, samples were metalized with a 20 nm platinum layer sputtered by physical vapor deposition (PVD). Then, they were fixed to the FIB chuck using copper scotch to ensure electrical contact between the top of the sample and the chuck. This step is crucial, especially on highly insulating sapphire substrates, to avoid important drift during the milling of the lamella.

Preparation of the lamella involves the following steps: 1) Deposition of two in-situ capping Pt layers using a gas injection system (GIS), the first layer is done with the electron beam, and a second thicker layer is deposited with the gallium ion beam. 2) lamella milling, 3) lift-out, 4) lamella transfer and fixing onto the TEM grid, 5) lamella thinning with progressive reduction of tension / current, starting at 30 kV, 0.79 nA, then at 30 kV, 0.23 nA, with a final thinning at 16 kV, 0.15 nA, 6) de-amorphization step performed at 2 kV, 23 pA.

TEM observations were conducted on an FEI Tecnai Osiris operating at 200 kV in STEM mode, using Bright Field (BF) and High-Angle Annular Dark-Field (HAADF) detectors. Energy Dispersive X-ray analysis (EDX) was also performed at 200 kV using four Bruker Silicon Drift Detectors (SDD).

To ensure uniform grayscale and enhance contrast across images, all Scanning Electron Microscopy (SEM) images underwent post-processing using a contrast-limited adaptive histogram equalization (CLAHE) algorithm from the Python OpenCV library.

## 3. Experimental results

### 3.1. $Cl_2$ plasma etching

a) Impact of pressure

Figure 2 shows AlN, SiN, and $SiO_2$ etch rate evolution as a function of chamber pressure as well as the resulting etch selectivity (corresponding to experiments 1 to 4 in Table 1). Increasing the pressure at fixed ion energy leads to decreasing etch rates for all materials. For any plasma conditions, as will be observed in the next sections, AlN is always etched 3-4 times faster than SiN and 6-12 times faster than $SiO_2$. However, the $SiO_2$ etch rate decrease with increasing pressure is more pronounced than the ones of AlN and SiN, which evolve quite similarly with pressure. The consequence is an AlN/$SiO_2$ etch selectivity increases with increasing pressure, while the AlN/SiN etch selectivity remains almost constant. The etch decrease may be explained by an electronic temperature decrease with pressure that leads to less ionization process and thus lower ion flux compared to neutral flux [27], as it will be discussed later.

Regarding the AlN pillar profiles shown in Figure 2, they turned from tapered (3-6°) at a 10 mTorr pressure to anisotropic (~1°) at a higher pressure of 30 mTorr. Moreover, it is clearly observed some deposits on the pattern sidewalls that can be removed with HF 50%. After passivation layer removal, the pillar keeps globally

the same profiles as the ones obtained before HF. All patterns present some top-edge striated damage. This is caused by the ionic bombardment that transfers the initial HM striated roughness into the AlN layer [31,32]. The damage seems more pronounced at low pressure consistently with higher ionic flux. Finally, it is observed that by increasing the pressure, the sidewalls turn into smooth crystalline facets oriented along the *a*-plane more easily.

b) Impact of bias power

Figure 3 shows that AlN, SiN, and $SiO_2$ etch rates increase with increasing bias power (experiments 3, 5, and 6 in Table 1), certainly due to improved sputter desorption of etch products from the surface. Again, the increase with bias is more enhanced for $SiO_2$ than AlN and SiN, resulting in lower $AlN/SiO_2$ and almost constant AlN/SiN etch selectivities with increasing bias power. The comparison of the pillar profiles before and after HF reveals that thicker passivation layers are present at lower bias. However, the pillar profiles turn from almost anisotropic (0.5-1.5°) at low bias power (80 W, ion energy of about 338 eV) to slightly tapered (1.5-3°) at higher bias power (200W, ion energy of 466 eV). At low bias, smooth *a*-faceting is visible on almost all the pattern heights.

c) Impact of source power

Figure 4 shows that AlN, SiN, and $SiO_2$ etch rates increase with increasing source power (experiments 3, 7, and 8 in Table 1), attributed to the simultaneous increase of ion and radical fluxes. $SiO_2$ etch rate is the more sensitive to this increase explaining why the $AlN/SiO_2$ selectivity decreases with increasing source power while AlN/SiN etch selectivity remains constant. Although the passivation layer thickness (measured at its maximum) is about the same for the three source conditions. The AlN profiles evolve from almost anisotropic (1° without considering the foot) at low source power (200 W) to tapered (2-3.5°) at high source power (800 W).

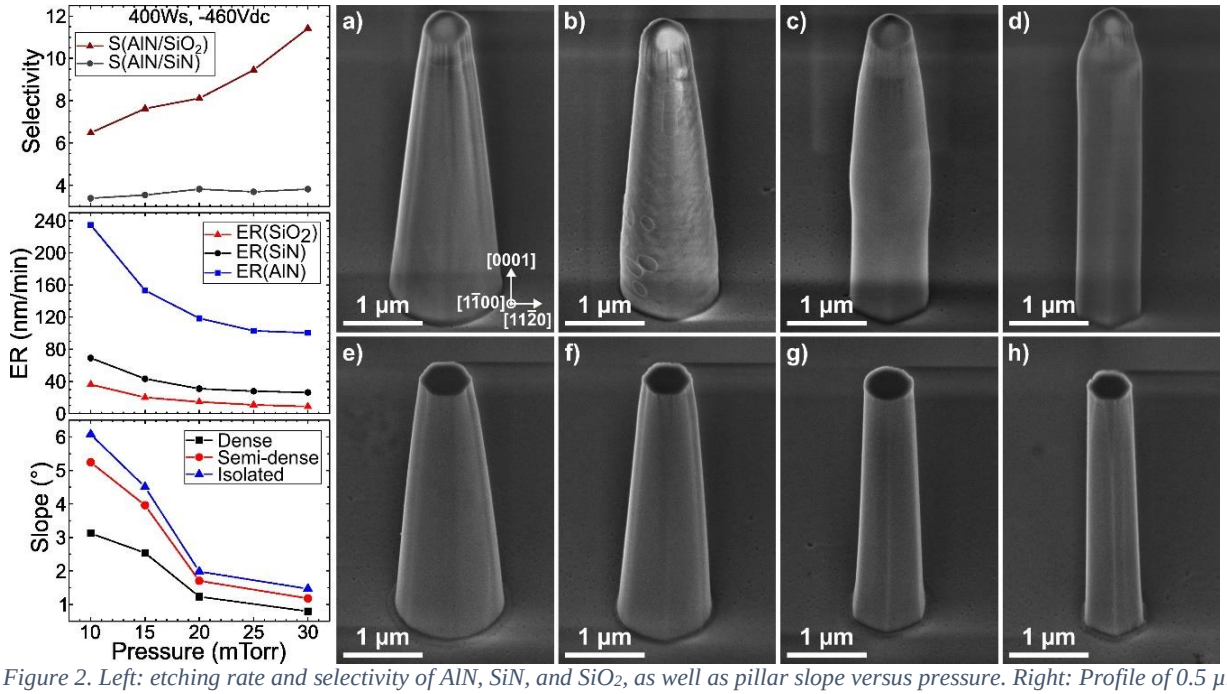


*Figure 2. Left: etching rate and selectivity of AlN, SiN, and $SiO_2$, as well as pillar slope versus pressure. Right: Profile of 0.5 µm m-oriented AlN pillars after a), b), c), d) plasma etching done at 400 W of source power, -460 $V_{DC}$, and a pressure of 10 mTorr, 15 mTorr, 20 mTorr, 30 mTorr, respectively (conditions 1, 2, 3, and 4 from Table1). e), f), g), h) Same pillars as a), b), c), d) after passivation and HM removal using HF 50% for 5 minutes.*

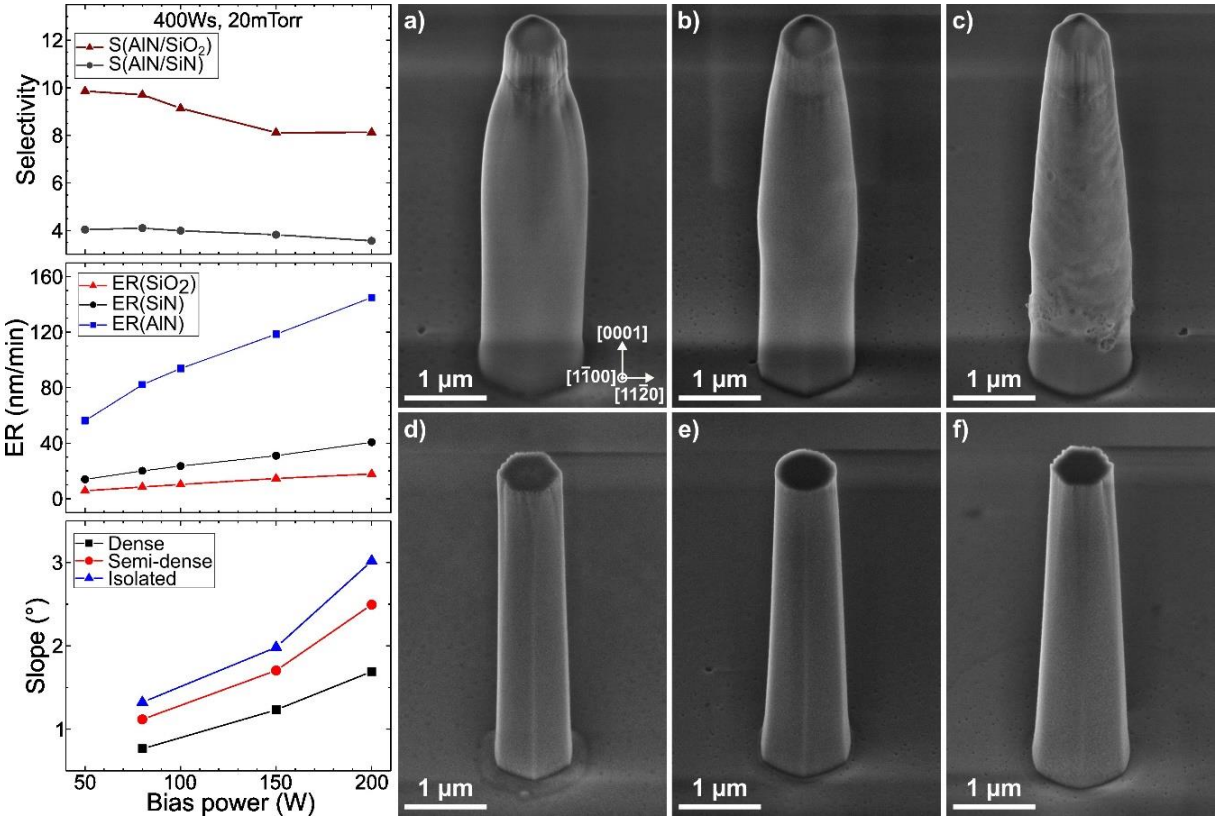


*Figure 3. Left: etching rate and selectivity of AlN, SiN, and $SiO_2$, as well as pillar slope versus bias power. Right: Profile of 0.5 µm m-oriented AlN pillars after a), b), c) plasma etching done at 20 mTorr pressure, 400 W of source power, and a bias power of 80 W, 150 W, and 200 W, respectively (conditions 5, 3, and 6 from Table1). d), e), f) Same pillars as a), b), c) after passivation and HM removal using HF 50% for 5 minutes.*

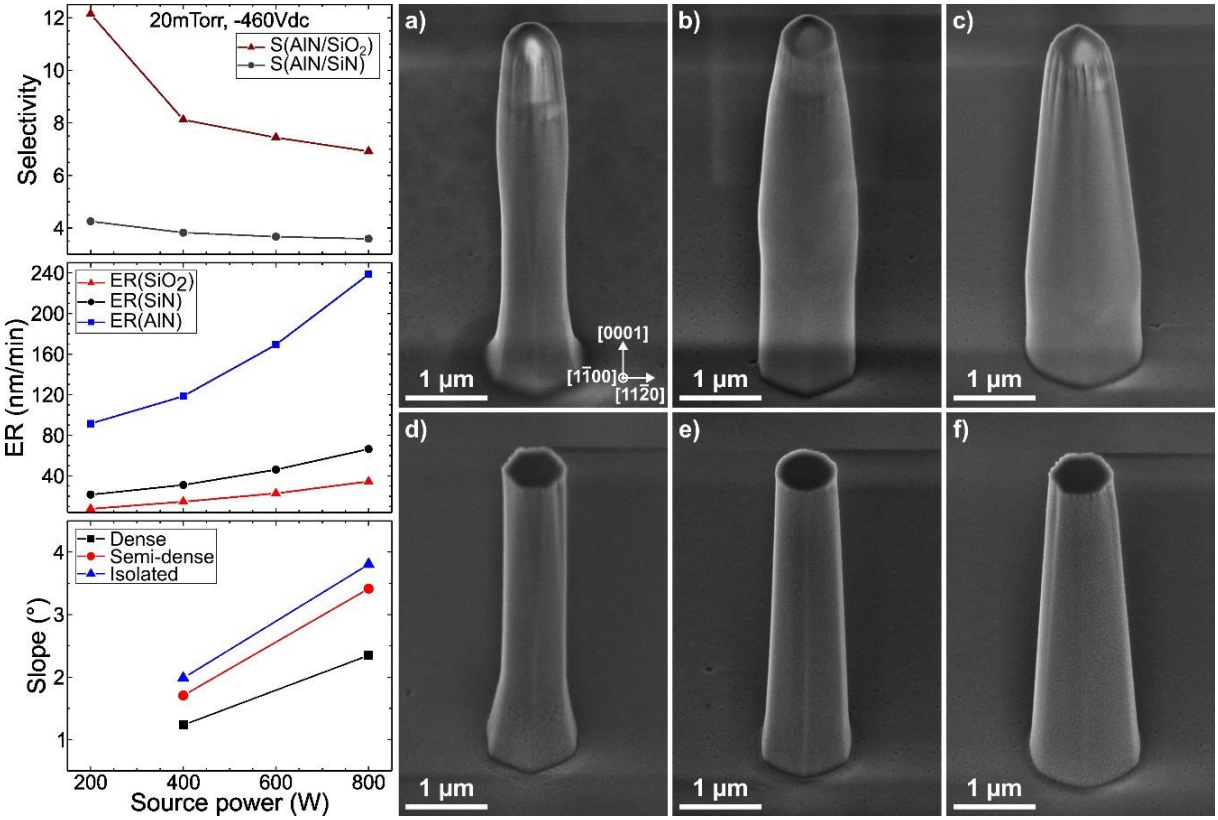


*Figure 4. Left: etching rate and selectivity of AlN, SiN, and $SiO_2$, as well as pillar slope versus source power. Right: Profile of 0.5 µm m-oriented AlN pillars after a), b), c) plasma etching done at 20 mTorr pressure, -460 $V_{DC}$, and a source power of 200 W, 400 W, and 800 W, respectively (conditions 7, 3, and 8 from Table1). d), e), f) Same pillars as a), b), c) after passivation and HM removal using HF 50% for 5 minutes.*

d) Discussion

In pure $Cl_2$ plasma, the main chemical active species are the Cl atoms while the physical sputtering is expected from $Cl_2^+$ and $Cl^+$ [27,33]. For any materials, including the ones under investigation here, the domination of a particular etch mechanism in $Cl_2$ plasma will depend on the total ion flux ($\Gamma_+$) / radical flux ($\Gamma_{Cl}$) ratio, combined with the ion energy. Efremov et al [27] showed in their

simulations that the $\Gamma_+/\Gamma_{Cl}$ ratio considerably decreases with pressure increase from 5 mTorr to 30 mTorr. At a fixed pressure, increasing the source power increases the ionization and dissociation processes and thus $\Gamma_{Cl}$ and $\Gamma_+$ simultaneously, but the $\Gamma_+/\Gamma_{Cl}$ increases. At fixed pressure and source power, it is generally admitted that an increase of bias power does not change the total ion flux, while $\Gamma_{Cl}$ can slightly decrease since Cl atoms are more consumed for the etching (loading effect), meaning that at higher bias $\Gamma_+/\Gamma_{Cl}$ ratio may increase.
Based on their simulations, it can be concluded that plasma conditions that favour higher $\Gamma_+/\Gamma_{Cl}$ (higher source power, lower pressure, and higher DC bias) enhance the etching of $SiO_2$, SiN, and AlN. Their etching in $Cl_2$ plasma follows an ion-enhanced chemical etching mechanism, meaning that higher ion flux and energy improve bond breaking before reaction with Cl radicals and also desorption of etch products from the surface.

According to the plasma conditions used in our study, the etch rates of AlN range from 60 to 240 nm/min which is in agreement with other studies dealing with AlN etching in $Cl_2$-based plasmas [15–23]. AlN is etched 3-4 times faster than SiN, itself etched 2-3 times faster than $SiO_2$.
Moreover, we observed that under the same plasma conditions, a GaN sample is etched 1.3 to 1.8 times faster than AlN samples [26]. The observed etch rate ranking GaN > AlN > SiN > $SiO_2$ is well consistent with the bond energy ranking [23,34,35]: GaN (2.24 eV) < AlN (2.88 eV) < SiN (3.7 eV) < $SiO_2$ (4.68 eV) and high-ion driven etching mechanisms where the bond breaking is the rate-limiting step of the whole reaction with the surface.
Once the Al-N bond is broken by the ionic bombardment, the Cl radicals are absorbed on the dangling
bonds (DB) of Al (or N atoms), creating a chemical reaction associated with the formation of volatile etched by-products ($AlCl_3$, $NCl_3$, $N_2$, …). Note that in the case of GaN etching in $Cl_2$ conditions, the etch by-products identified by mass spectrometry or optical emission measurements were $GaCl_x$ or $N_2$ species even if they do not exclude the possibility to form $NCl_3$ products [36].
It is also worth mentioning that without energetic ionic bombardment, there is no spontaneous chemical etching driven by Cl radicals. Indeed, we exposed the sloped patterns of Figure 2-e to a 10 mTorr or 30 mTorr $Cl_2$ plasma without any bias (ion energy of about 15-20 eV) for 3000 seconds. No profile change or etching was observed either on the sidewalls or the *c*-plane (not shown here), meaning that a minimum ion energy is required to activate the etch mechanisms and that chlorine radicals alone cannot lead to a lateral etching.

Regarding the AlN pattern profiles, it is also observed that plasma conditions that favour higher $\Gamma_+/\Gamma_{Cl}$ (higher source power, lower pressure, and higher bias power) lead to tapered AlN profiles. On the contrary, conditions that favour higher radical flux over ion flux (such as pressure increase or source power decrease) allow obtaining anisotropic pillars with smooth *a*-facetted sidewalls.
TEM and EDX analyses (cf. Figure 5) performed after AlN etching at 20 mTorr on 1 µm-diameter semi-dense pillars confirm the presence of a passivation layer on the AlN sidewalls, with a thickness at its maximum (1-2 µm below the hard mask) of 50-55 nm and almost no passivation at the pillar base. This redeposit layer is mainly composed of Silicon, Oxygen, and Aluminium (cf. Fig 5-c to 5-g). The Silicon comes from the carrier wafer etching and the presence of oxygen is attributed to the Si oxidation due to air exposure. Aluminium most likely originates from the AlN sample. No Chlorine was detected, certainly because of its substitution by oxygen under air exposure. The presence of Nitrogen is hard to assert due to the low sensitivity of light elements in EDX analysis.
These results suggest that the deposition mainly comes from the etching of the SiN carrier wafer and that the SiN etch by-products (typically SiClx, NClx species) redeposit from the plasma on the pillar sidewalls. Generally, the thickness of the passivation layer formed by redeposition from the plasma phase on the pattern sidewalls is thicker at the top and gradually decreases along the pattern height. But as the top pattern is more subjected to ionic bombardment, the passivation layer is more sputtered, explaining why the maximal thickness is at the pillar middle. This is also why it is difficult to draw a direct link between the thickness of the passivation layer and the pattern anisotropy. However, Figure 6 clearly shows a link between the SiN CW etch rate and the sidewall slope. The higher the SiN etch rate, the greater the slope, suggesting that the deposition of SiN etch by-products coming from the plasma phase on the AlN pillar sidewalls plays a major role in the AlN pattern profile. Moreover, dense AlN pillars are always straighter than isolated ones, consistently with a lower collection angle of neutral depositing species in dense than in isolated patterns (Figure 6).

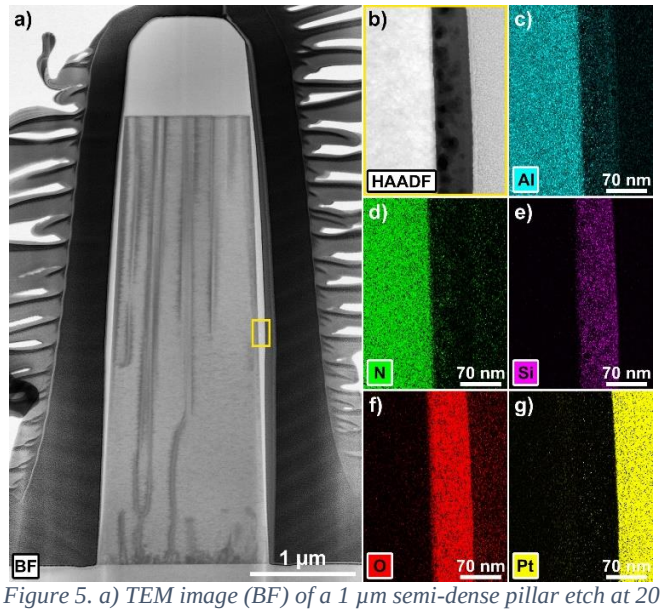

*Figure 5. a) TEM image (BF) of a 1 µm semi-dense pillar etch at 20 mTorr (condition 3 from Table 1), yellow rectangle indicates the area of EDX analysis. b) TEM image (HAADF) of the passivation layer where EDX analysis is performed. c), d), e), f), g), h) EDX*

*analysis showing the presence of Al, N, Si, O, and Pt, respectively. The Pt element come from the capping layer.*

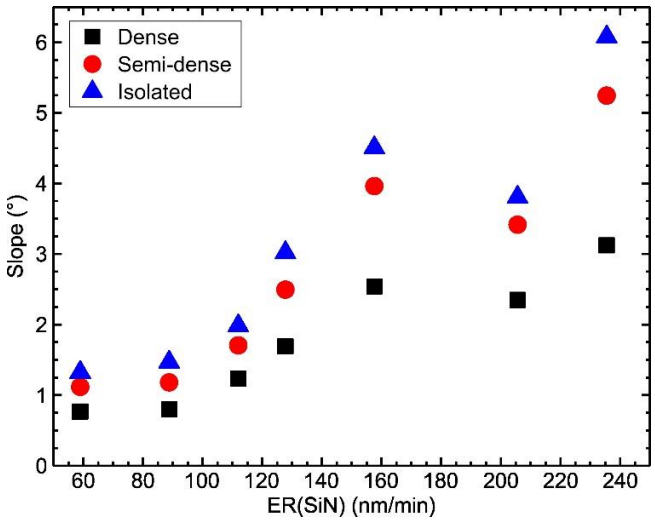


*Figure 6. The slope of the pillars in ° (for different pitches) as a function of the SiN etching rate.*

However, even if the deposition from the gas phase plays a role in the AlN profile, other mechanisms may take place. The presence of Al in the deposit (cf. Figure 5) suggests some line-of-sight deposition of products sputtered from the AlN bottom to the pillar sidewalls [37,38]. Such deposition mechanism is known to generate pattern slope by slowing down the lateral etch progression [37]. Moreover, higher ionic bombardment leads to a higher amount of sputtered species and consequently more important slope. This mechanism may also contribute to the slope formation that we observe for a high $\Gamma_+ / \Gamma_{Cl}$ ratio.

Another phenomenon that may drive the pattern slope is the crystal orientation-dependent etching effect. Coulon et al [39] investigate the impact of $Ar/Cl_2$ plasma etching conditions on the etch rate and the morphology of GaN nanorods patterned from GaN substrates with different orientation planes (polar (0001), Semi-Polar (1122) and Non-Polar (1120)). They observe that for any of their plasma conditions, *a*-semipolar horizontal planes are etched faster than *a*-nonpolar ones, which themselves are etched faster than *c*-planes. Moreover, plasma conditions for which the chemical component of the plasma dominates lead to different nanorod profiles according to the initial orientation plane of the substrate, highlighting some crystal orientation-dependent etching mechanisms. In contrast, increasing the physical component enables to minimize the impact of crystal orientation.
AlN has the same Wurtzite crystal structure as GaN with identical hexagonal geometry. It is likely that similar mechanisms drive its etching.

From this understanding of the crystallographic preferential etching combined with the formation of the passivation layer, we can propose a model explaining the pattern profiles. During the etching, pillar profiles (i.e. pillar slope) are driven by the crystallographic preferential etching, which is dependent on the $\Gamma_+ / \Gamma_{Cl}$ ratio and ion energy.

For conditions that minimize the ionic bombardment (low $\Gamma_+ / \Gamma_{Cl}$ ratio, or low ion energy), the *c*-horizontal plane may etch more slowly compared to the oblique semipolar plane. With a semipolar/polar etching rate ratio >> 1, the pillar profiles tend to be straightened during the etching. Additionally, a low ionic bombardment induces a lesser passivation formation, leaving more time for the plasma to straighten the sidewalls (cf. Fig. 7-a). Overall, in this configuration, the lateral progression of the etch will stop as soon as a vertical nonpolar facet is reached since those surfaces are no longer subjected to the ionic bombardment mandatory to activate the etching. This led to the formation of straight pillars.
For higher ionic bombardment (high $\Gamma_+ / \Gamma_{Cl}$ ratio, or high ion energy) the etching of the *c*-plane is enhanced and may be equivalent to the semipolar one due to the stronger physical nature of the plasma. In this situation, a semipolar/polar etching rate ratio ≈ 1 could lead to the formation of more tapered profiles during the etching. Additionally, at high ionic bombardment, more passivation comes from the gas phase, and/or the line of sight is formed on pillar sidewalls. This will shield the pillars from any further sidewall lateral etching keeping their profile tapered (cf. Fig. 7-b). This latter mechanism is most likely responsible for the profile difference observed on different pillar densities shown in Figure 6. Indeed, in dense arrays, the formation of a passivation layer coming from the gas phase is slower due to the shadowing, leaving more time for the plasma to straighten the profiles.

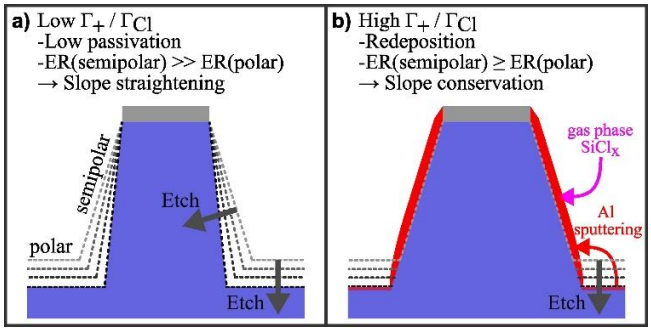


*Figure 7. Illustration of a), b) the impact of a low/high $\Gamma_+ / \Gamma_{Cl}$ ratio on the passivation formation and its impact on pillar profiles. Grey arrows and dashed lines indicate the etching progression.*

Finally, all the plasma etching results shown above were performed with the *m*-oriented hard mask. However, similar pattern profiles with plasma conditions were observed with the *a*-oriented hard mask. The slight difference is in the *a*-facet appearance. For both hard mask shapes and all plasma conditions, the appearance of *a*-facet is visible at the pattern bottom, but in the case of *a*-oriented hard mask, the *a*-facets are well defined from the top to the bottom of the pattern. This trend was also observed with the patterning of GaN pillars in $Cl_2$ plasma [26]. The *a*-facet formation is also favoured for plasma conditions using low $\Gamma_+ / \Gamma_{Cl}$. These observations suggest that *m*-type semipolar planes are etched faster than *a*-type ones and thus less stable. This was also observed by Okada in the case of GaN trench etching in $Cl_2$ plasma [40]. The etch propagates parallel to *a*-type

oblique semipolar plane until the corresponding vertical nonpolar *a*-plane is reached.
This preliminary section highlights that homogeneous arrays of anisotropic AlN pillars of various densities and diameters can be obtained with nicely defined *a*-facet if an *a*-oriented hard mask is used combined with a $Cl_2$ plasma showing low ionic bombardment (i.e either low $\Gamma_+ / \Gamma_{Cl}$ or low ion energy). Such conditions are obtained by operating at either low source power, high pressure, or low bias power. Note that in the present case, high ionic bombardment favors two mechanisms that can lead to slope generation: 1) the redeposition of SiN etch byproducts and 2) the minimization of crystallographic preferential etching, and thus it is hard to identify which mechanisms dominate the slope generation. Figure 8 illustrates the quality of the patterning that can be obtained at high pressure (30mT): 500nm diameter pillars with smooth *a*-facet and a slope of about 1° for all densities.
However, due to the inability to obtain the desired *m*-oriented sidewalls through plasma etching alone, the capability of post-plasma etching wet KOH treatment was investigated.

### 3.2. Wet etching

44% KOH wet treatments with various durations were performed on AlN pillars patterned with the following plasma parameters: 190 sccm of $Cl_2$, 10 mTorr pressure, 400 W of source power, and 220 W of bias power (equivalent to a DC bias of -460 V) as shown in Figure 2-a. These conditions were purposely selected to obtain tapered AlN profiles. Indeed, in our previous study [30], regarding GaN pillar fabrication with a two-step process combining dry and KOH wet etching, we demonstrated that the pattern profile plays a key role in the efficiency of the wet treatment. If the pillars have a fully anisotropic or a re-entrant profile, the sidewalls composed of non-polar planes remain stable and unetched during the KOH treatment. Our conclusion was that for an efficient post-etch KOH treatment, the pillar profile should present some slopes.

a) Role of the HM

The impact of the wet treatment was investigated on AlN pillars with the HM removed by a 50% HF solution and on pillars with HM still in place but with the passivation layer removed with a 1% HF solution (cf. Figure 9).
In either case, the wet etching propagates both vertically and horizontally, resulting in the formation of a rough staircase pattern on the tapered sidewalls composed of *c*- and *m*-planes. The *m*-planes exhibit a prism-like shape with a 120° angle between two adjacent *m*-planes. The absence of *a*-planes indicates that they are etched faster than the *m*-planes, leading to their complete disappearance [41].
This experiment also illustrates the significant role played by the HM during the wet process. Without HM, the top *c*-plane horizontal surface of the pillar remains stable over time during the wet process (cf. Fig. 9-a and 9-b), while the top edges of the pillar are laterally eroded. The upper part of the pillars shrinks at a rate of around 110 to 130 nm/min, corresponding to a horizontal etching rate of approximately 55-65 nm/min. With increased wet duration, the ultimate shrinkage of the pillar diameter at the top results in the disappearance of the horizontal *c*-plane (cf. Fig. 9-c and 9-d).
In contrast, the presence of the HM prevents the extension of horizontal etching at the top edge of the pillar as shown in Figure 9-f to 9-j. At the same time, the tapered sidewalls are etched both vertically and horizontally by the KOH. The tapered area reduces in height with increased KOH duration, nearly vanishing after 3 minutes of wet etching. The etching progression of the tapered area can vary from one pillar to another, making it difficult to provide a precise value. However, the vertical etching rate appears to be around 1 to 1.5 µm/min. The vertical etching progresses until the sapphire substrate is reached, while the horizontal etching stops when reaching the stable nonpolar planes defined by the HM (*m*-planes in the present case), allowing an anisotropic transfer of the HM into the pillars in 6 to 10 minutes as illustrated in Figure 9-i. It is worth mentioning that here pillar slope value is 0°, indicating that the pillars are completely straight whatever the initial hard mask shape.

If we extend the wet duration even further, up to 40 minutes (cf. Fig. 9-j), the nonpolar planes revealed by the KOH are not etched at all, confirming their stability.

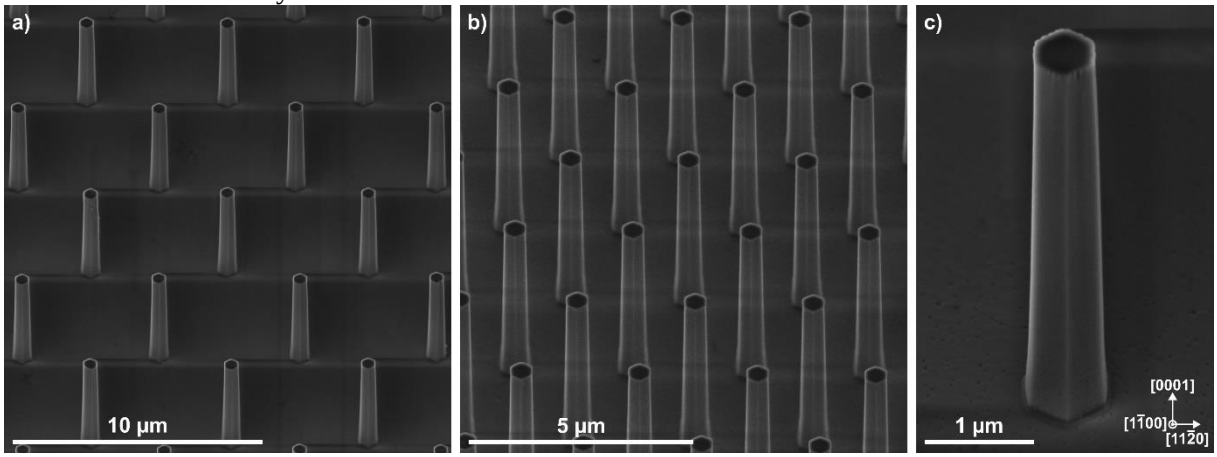


*Figure 8. SEM images of a-oriented pillars of 0.5 µm diameters after plasma etching (30 mTorr, condition n°4 of Table 1) and HM removal using HF 50%. a) Semi-dense array, b) dense array, c) zoom on a single pillar of the semi-dense array.*

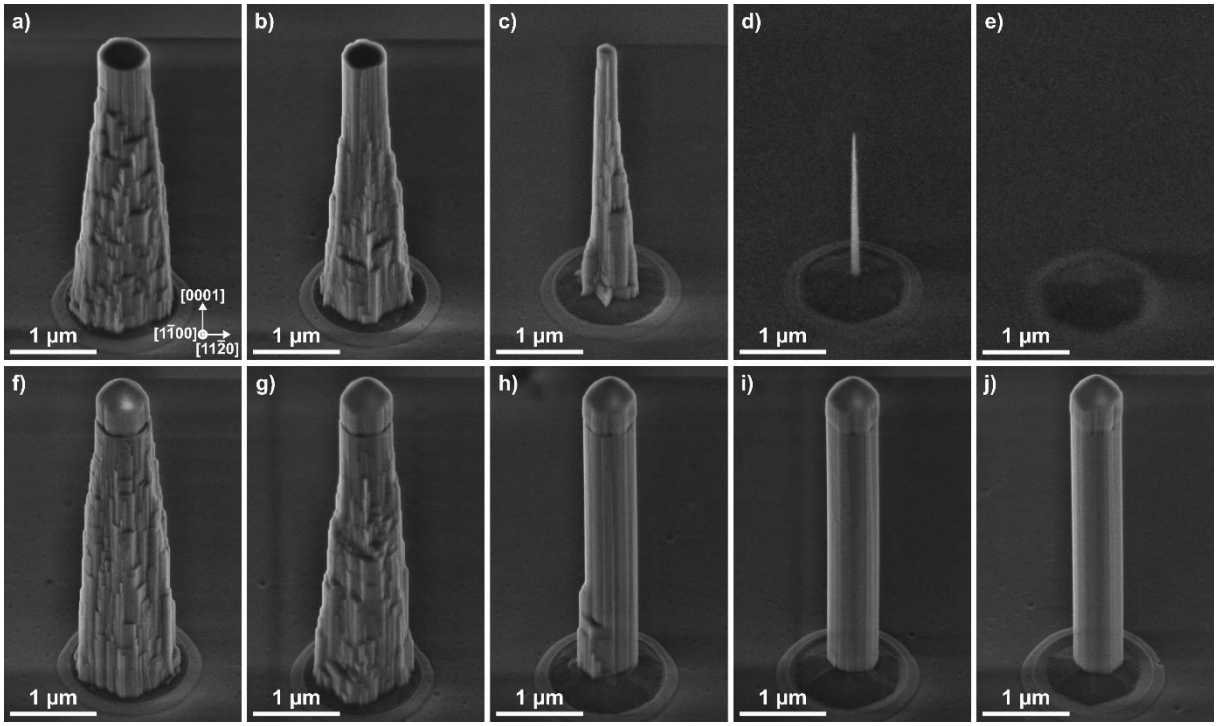


*Figure 9. SEM images of m-oriented pillars of 500 nm diameters a)-e) without and f)-j) with HM, exposed to a 44% KOH wet treatment during: a), f) 20s, b), g) 60s, c), h) 180s, d), i) 360s, and e), j) 40 minutes.*

AlN etching with KOH only occurs on the unprotected sidewalls and at the top edges of the pillars when no HM is present, more precisely at the polar/nonpolar plane intersection. The use of an HM to protect the vulnerable upper top areas prevents any vertical or lateral etching at the top of the pillar [42], leaving only the tapered sidewalls etched by the wet, allowing the transfer of the HM shape onto the pillar.

b) Impact of the HM shape

Finally, we also notice a difference in sidewall morphologies after KOH wet etching depending on the HM shape used. When using an *m*-oriented HM, pillar sidewalls are remarkably smooth throughout the entire pattern height with just a few terraces between the different *m*-planes (cf. Fig. 10-a). When using an *a*-oriented HM, pillar sidewalls are rougher with the presence of vertical prism-like striations on the entire pattern height (cf. Fig. 10-b). These zig-zag lines closely follow the HM striations, formed during the AlN plasma etching. This morphological difference between *m*- and *a*-oriented pillars is similar to what we already observed during the KOH wet etching of GaN [30]. That combined with the fact that KOH reveals *m*-planes lets us think that *m*- and *a*-oriented pillars sidewalls are both composed of *m*-facets only. These facets form large and smooth *m*-planes in the case of *m*-oriented HM or a rough succession of prism-like triangles in the case of *a*-oriented HM.

Note that in this work, the pillar profile was strongly tapered (using the 10m Torr etching recipe shown in Fig. 2-a) in order to better visualize the wet etching behavior but completely similar results were observed on pillarswith slightly tapered profile (using the 20 mTorr etching recipe shown in Fig. 2-c).

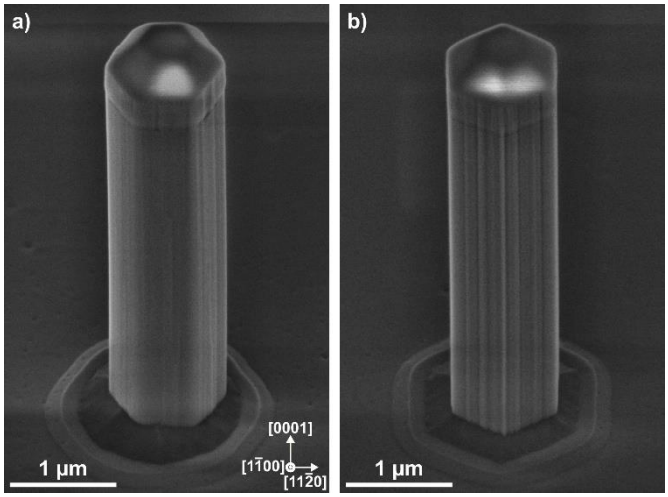


*Figure 10. a), b) SEM images of 1 µm diameter pillars with m-oriented and a-oriented HM respectively after plasma etching and 10 min of 44% KOH wet treatment.*

**Discussion on the comparison between KOH etching and $Cl_2$ plasma etching of AlN and GaN**

Consistently with the literature, we observed that AlN is etched about 40 times faster than GaN with wet KOH solution [30,43–45]. In contrast, AlN is etched 1.3-1.8 times slower than GaN in $Cl_2$ plasma [15–23,26]. Moreover, both $Cl_2$ plasma and wet KOH processes are driven by crystal orientation preferential etching but the stable crystallographic planes are different. Usually, the most stable planes are those that are etched the slowest. Wet KOH solution reveals *c*- and *m*-type planes, while $Cl_2$ plasma conditions with dominant chemical components (low $\Gamma_+/\Gamma_{Cl}$ ratio and low ion energy) favour the apparition of *a*-type planes.

All these trends can be well understood from the literature.

The wet etching mechanisms of AlN and GaN in KOH solution assume the oxidation of the metal atom (Al or Ga) via hydroxide ($OH^-$) molecules attacking and

breaking the Metal-N bonds, freeing the metal atom to oxidize into $Al_2O_3$ or $Ga_2O_3$ which are then dissolved as described in equation (1) and (2) [46,47].

$$2AlN + 3H_2O \xrightarrow{KOH} Al_2O_3 + 2NH_3 \quad (1)$$

$$2GaN + 3H_2O \xrightarrow{KOH} Ga_2O_3 + 2NH_3 \quad (2)$$

The faster etch rate of AlN in KOH solution was attributed to an easier formation and better dissolution of $Al_2O_3$ compared to $Ga_2O_3$ [47]. Contrary to $Cl_2$ plasma etching, the breakage of atomic bonds between metal atoms and nitrogen atoms is not the rate-limiting step of the whole reaction in the KOH wet process. Lai et al. [48] proposed a physical quantity called *etching barrier index* (EBI), which is the product of planar atom density by the number of dangling bonds per nitrogen atom in a plane, to describe the etching resistivity of each GaN plane in an alkaline etching solution. The higher the EBI value of a plane is, the more difficult the etching of this plane would be. Indeed, the negative charge of N dangling bonds (DB) repels the $OH^-$ ions and prevents them from approaching the Metal–N bonding at the second layer. Here it is important to precise that this EBI model is an approximation of the plane stability under KOH etching and does not take into account other parameters such as spontaneous polarization or surface energies.

Although *a*-nonpolar planes are denser, the fact that the N atoms present on the plane have 1 DB (vs 2 DB for *m*-plane, and 3 DB for *c*-plane) makes them less stable to wet KOH etching and disappear faster than *m*-planes. This trend is also true for semipolar planes with *a*-semipolar exhibiting a lower EBI compared to *m*-semipolar. Additionally, semipolar planes have a lower EBI than nonpolar planes, making them much less resistant to KOH etching, and thus explaining their quick disappearance (cf. Table 2).

Concerning the number of nitrogen DB per plane, Kazanowska et al. [49] note that due to the asymmetric nature of the atomic stacking within the AlN crystal, some planes (in Table 2 the *m*-nonpolar and the *a*- and *m*-semipolar planes) can have 1 or 2 DB depending on the positioning of the plane in the crystal. To solve this issue, Kazanowska et al. use a fractional number of DB (1.27 for those three families of planes). In our case, we assume that it is the highest number of DB per plane that will be the limiting factor for the etching capability of a plane so we keep the value of 2 DB for *m*-nonpolar, *a*-semipolar, and *m*-semipolar planes. However, the reasoning and the relative etching ability of the planes remain similar for both DB values, with the following KOH wet etching robustness for the different planes: *c*-plane > *m*-nonpolar > *a*-nonpolar > *m*-semipolar > *a*-semipolar.

Regarding the $Cl_2$ plasma process, the metal-N bonds must physically be broken to generate dangling bonds on the metal atoms on which Cl radical can absorb until a volatile product such as $GaCl_3$ or $AlCl_3$ is formed. This implies that the etch capability of a plane will be mostly driven by the planar density of Al atoms, whereas planes with higher Al density require more Cl ions to break their bonds, and more Cl radicals to remove the Al atoms. The *c*-plane, with its higher Al density, is the harder plane to etch. Among the nonpolar planes, the *a*-plane exhibits a higher Al density than the *m*-plane and thus is the most robust. This difference leads to the formation of the *a*-facets on the pillar sidewalls. As the AlN bond energy is higher than the GaN one, AlN is etched at a lower etch rate. This simple model based on the Al planar density is just an approximation of the plane stability under $Cl_2$ plasma etching and does not take into account other parameters such as bond density.

*Table 2. Miller index, Number of Al atoms, density of Al atoms, density of atoms, number of DB per N atoms, and EBI for c-, a-, and m- nonpolar and semipolar planes in AlN wurtzite crystal.*

| Plane | Miller index | Number of atoms per plane | Al planar density (atom/Å²) | Density of atom (atom/Å²) | Number of DB per N atoms | EBI (1/ Å²) |
|---|---|---|---|---|---|---|
| *c*-plane | (0001) | 1 Al | 0.1033 | 0.1032 | 3 | 0.3096 |
| *a*-plane | $\{11\bar{2}0\}$ | 2 Al, 2 N | 0.0745 | 0.1490 | 1 | 0.1490 |
| *m*-plane | $\{10\bar{1}0\}$ | 1 Al, 1 N | 0.0645 | 0.1291 | 2 | 0.2582 |
| *a*-semipolar | $\{11\bar{2}2\}$ | 1 Al | 0.0316 | 0.0316 | 2 | 0.0632 |
| *m*-semipolar | $\{10\bar{1}1\}$ | 1 Al | 0.0547 | 0.0547 | 2 | 0.1095 |

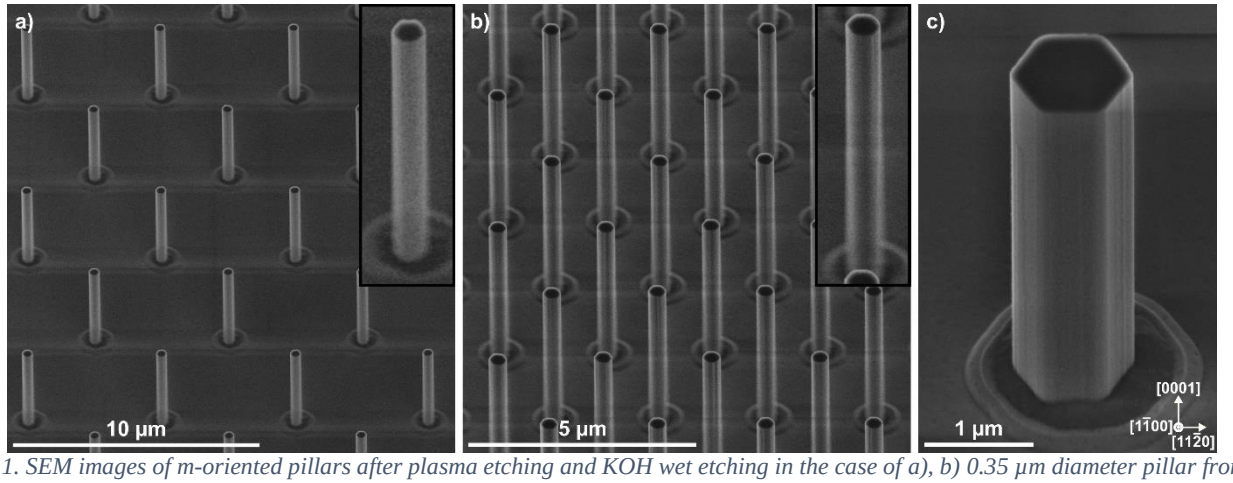


*Figure 11. SEM images of m-oriented pillars after plasma etching and KOH wet etching in the case of a), b) 0.35 µm diameter pillar from semi-dense and dense arrays respectively. For both images, a zoom on one pillar is shown in the top right corner. c) Zoom image on a 1 µm diameter pillar from the semi-dense array.*

## Conclusion

In this study, the authors demonstrate the feasibility of producing high aspect ratio (>10) AlN pillar arrays with anisotropic and *m*-oriented sidewalls using a two-step process that combines $Cl_2$ plasma etching and KOH wet etching (cf. Fig. 11).

The etching of AlN in $Cl_2$ plasma is highly driven by the ionic bombardment that is mandatory to break the strong Al-N bonds. It is also a crystallographically dependent process because the Al planar atomic density, and thus the number of AlN bonds to be broken is different between semipolar, nonpolar, and polar planes. The higher the Al content on a plane will lead to lower etch rate of the crystallographic plane. Thus, the ionic bombardment (ion flux / radical flux ratio ($\Gamma_+ / \Gamma_{Cl}$) and ion energy) plays an important role in the AlN etch rates, the pillar profiles, and sidewalls faceting. Higher ionic bombardment (high $\Gamma_+ / \Gamma_{Cl}$ ratio or high ion energy) leads to higher etch rates and also reduces the etching rate differences between the crystallographic planes limiting the appearance of a specific faceting. In contrast, low ionic bombardment (low $\Gamma_+ / \Gamma_{Cl}$ ratio or low ion energy) leads to lower vertical etch rate, straight profiles, and the appearance of *a*-faceting. The *a*-faceting formation rather than *m*-one may be explained by the fact that *m*-type planes are etched faster due to lower Al planar density. In addition to that, the ionic bombardment also drives the formation of a passivation layer on the pillar sidewalls coming from either the CW etch by-products ejected in the plasma or by an Al line of sight redeposition. For both mechanisms, higher ionic bombardment (high ion flux and/or energy) favors the formation of the passivation layer explaining why tapered profiles are more easily obtained in those conditions. By optimizing the plasma parameters to get low ionic bombardment (low source power, high pressure, or low bias power), AlN pillars with almost straight sidewalls (1°) can be obtained but unfortunately in those conditions, *a*-facets are favored.

To overcome the impossibility of obtaining *m*-oriented sidewalls with plasma etching, KOH wet etching post-plasma treatments were investigated. On anisotropic profiles, the KOH wet etching is ineffective, due to the high stability of the vertical non-polar planes. In contrast, tapered sidewalls (corresponding to semipolar planes) are vulnerable and can easily be etched by the KOH. Such vulnerabilities are also present at the intersection between polar and non-polar planes at the top of the pillars. This implies that the presence of the hard mask is mandatory to avoid damage and lateral etching at the top edge pillar. We also observed that the *m*- and *c*- planes are the most stable planes under wet KOH, implying that those planes are the ones that remain at the end of the wet process. Thus, the use of the HM during the wet treatment allows to etch all the tapered areas until the stable non-polar planes defined by the HM shape are reached. By using an *m*-oriented hexagonal HM shape, AlN pillars with anisotropic and smooth *m*-faceted sidewalls can be obtained.

In summary, based on all this understanding, the authors demonstrate the feasibility of producing high aspect ratio AlN pillars, which will serve as building blocks for core-shell UV-LEDs. The key parameters for this process involve the realization of tapered pillars using $Cl_2$ plasma etching, followed by a KOH wet etching step with a *m*-oriented HM still present at the top of the pillars.

## Acknowledgment

This research was funded by the French National Research Agency in the framework of the program ANR-22-CE51-0032-01 and the French National Research Agency in the framework of the "Investissements d'avenir" program (ANR-15-IDEX-02). It was also supported by the French RENATECH network.

[1] M. Kneissl, T.-Y. Seong, J. Han, H. Amano, The emergence and prospects of deep-ultraviolet light-emitting diode technologies, Nat. Photonics 13 (2019) 233–244. https://doi.org/10.1038/s41566-019-0359-9.
[2] C.R. Haughn, G. Rupper, T. Wunderer, Z. Yang, N.M. Johnson, M. Wraback, G.A. Garrett, Highly radiative nature of ultra-thin c-plane Al-rich AlGaN/AlN quantum wells for deep ultraviolet emitters, Applied Physics Letters 114 (2019) 102101. https://doi.org/10.1063/1.5087543.
[3] H. Amano, R. Collazo, C.D. Santi, S. Einfeldt, M. Funato, J. Glaab, S. Hagedorn, A. Hirano, H. Hirayama, R. Ishii, Y. Kashima, Y. Kawakami, R. Kirste, M. Kneissl, R. Martin, F. Mehnke, M. Meneghini, A. Ougazzaden, P.J. Parbrook, S. Rajan, P. Reddy, F. Römer, J. Ruschel, B. Sarkar, F. Scholz, L.J. Schowalter, P. Shields, Z. Sitar, L. Sulmoni, T. Wang, T. Wernicke, M. Weyers, B. Witzigmann, Y.-R. Wu, T. Wunderer, Y. Zhang, The 2020 UV emitter roadmap, J. Phys. D: Appl. Phys. 53 (2020) 503001. https://doi.org/10.1088/1361-6463/aba64c.
[4] C. Durand, C. Bougerol, J.-F. Carlin, G. Rossbach, F. Godel, J. Eymery, P.-H. Jouneau, A. Mukhtarova, R. Butté, N. Grandjean, *M*-Plane GaN/InAlN Multiple Quantum Wells in Core–Shell Wire Structure for UV Emission, ACS Photonics 1 (2014) 38–46. https://doi.org/10.1021/ph400031x.
[5] V. Grenier, S. Finot, L. Valera, J. Eymery, G. Jacopin, C. Durand, UV-A to UV-B electroluminescence of core-shell GaN/AlGaN wire heterostructures, Applied Physics Letters 121 (2022) 131102. https://doi.org/10.1063/5.0101591.
[6] S. Li, A. Waag, GaN based nanorods for solid state lighting, Journal of Applied Physics 111 (2012) 071101. https://doi.org/10.1063/1.3694674.
[7] Q. Li, J.J. Figiel, G.T. Wang, Dislocation density reduction in GaN by dislocation filtering through a self-assembled monolayer of silica microspheres, Appl. Phys. Lett. 94 (2009) 231105. https://doi.org/10.1063/1.3152012.
[8] P.-M. Coulon, B. Alloing, V. Brändli, P. Vennéguès, M. Leroux, J. Zúñiga-Pérez, Dislocation filtering and polarity in the selective area growth of GaN nanowires by continuous-flow metal organic vapor phase epitaxy, Appl. Phys. Express 9 (2016) 015502. https://doi.org/10.7567/APEX.9.015502.
[9] T. Onuma, H. Amaike, M. Kubota, K. Okamoto, H. Ohta, J. Ichihara, H. Takasu, S.F. Chichibu, Quantum-confined Stark effects in the m-plane $In_{0.15}Ga_{0.85}N$/GaN multiple quantum well blue light-emitting diode fabricated on low defect density freestanding GaN substrate, Appl. Phys. Lett. 91 (2007) 181903. https://doi.org/10.1063/1.2802042.
[10] M. Djavid, Z. Mi, Enhancing the light extraction efficiency of AlGaN deep ultraviolet light emitting diodes by using nanowire structures, Appl. Phys. Lett. 108 (2016) 051102. https://doi.org/10.1063/1.4941239.
[11] V. Grenier, S. Finot, B. Gayral, C. Bougerol, G. Jacopin, J. Eymery, C. Durand, Toward Crack-Free Core–Shell GaN/AlGaN Quantum Wells, Crystal Growth & Design 21 (2021) 6504–6511. https://doi.org/10.1021/acs.cgd.1c00943.
[12] J. Zheng, Y. Yang, B. Yu, X. Song, X. Li, [0001] Oriented Aluminum Nitride One-Dimensional Nanostructures: Synthesis, Structure Evolution, and Electrical Properties, ACS Nano 2 (2008) 134–142. https://doi.org/10.1021/nn700363t.
[13] R.G. Banal, M. Funato, Y. Kawakami, Surface diffusion during metalorganic vapor phase epitaxy of AlN, Phys. Status Solidi (c) 6 (2009) 599–602. https://doi.org/10.1002/pssc.200880415.
[14] K. Zhang, T. Takahashi, D. Ohori, G. Cong, K. Endo, N. Kumagai, S. Samukawa, M. Shimizu, X. Wang, High-quality nanodisk of InGaN/GaN MQWs fabricated by neutral-beam-etching and GaN regrowth: towards directional micro-LED in top-down structure, Semicond. Sci. Technol. 35 (2020) 075001. https://doi.org/10.1088/1361-6641/ab8539.
[15] P. Coulon, G. Kusch, E.D. Le Boulbar, P. Chausse, C. Bryce, R.W. Martin, P.A. Shields, Hybrid Top-Down/Bottom-Up Fabrication of Regular Arrays of AlN Nanorods for Deep-UV Core–Shell LEDs, Physica Status Solidi (b) 255 (2018) 1700445. https://doi.org/10.1002/pssb.201700445.
[16] F.A. Khan, L. Zhou, V. Kumar, I. Adesida, R. Okojie, High rate etching of AlN using BCl3/Cl2/Ar inductively coupled plasma, Materials Science and Engineering: B 95 (2002) 51–54. https://doi.org/10.1016/S0921-5107(02)00160-5.
[17] V. Bliznetsov, B.H.B. Johari, M.T. Chentir, W.H. Li, L.Y. Wong, S. Merugu, X.L. Zhang, N. Singh, Improving aluminum nitride plasma etch process for MEMS applications, J. Micromech. Microeng. 23 (2013) 117001. https://doi.org/10.1088/0960-1317/23/11/117001.
[18] X. Liu, C. Sun, B. Xiong, L. Niu, Z. Hao, Y. Han, Y. Luo, Smooth etching of epitaxially grown AlN film by Cl2/BCl3/Ar-based inductively coupled plasma, Vacuum 116 (2015) 158–162. https://doi.org/10.1016/j.vacuum.2015.03.030.
[19] M.A. Miller, M.H. Crawford, A.A. Allerman, K.C. Cross, M.A. Banas, R.J. Shul, J. Stevens, K.H.A. Bogart, Smooth and Vertical Facet Formation for AlGaN-Based Deep-UV Laser Diodes, Journal of Elec Materi 38 (2009) 533–537. https://doi.org/10.1007/s11664-009-0670-1.
[20] S.A. Smith, C.A. Wolden, M.D. Bremser, A.D. Hanser, R.F. Davis, W.V. Lampert, High rate and selective etching of GaN, AlGaN, and AlN using an inductively coupled plasma, Appl. Phys. Lett. 71 (1997) 3631–3633. https://doi.org/10.1063/1.120463.

[21] Jewon Lee, Hyun Cho, D.C. Hays, C.R. Abernathy, S.J. Pearton, R.J. Shul, G.A. Vawter, J. Han, Dry etching of GaN and related materials: comparison of techniques, IEEE J. Select. Topics Quantum Electron. 4 (1998) 557–563. https://doi.org/10.1109/2944.704117.
[22] S.J. Pearton, R.J. Shul, F. Ren, A Review of Dry Etching of GaN and Related Materials, MRS Internet j. Nitride Semicond. Res. 5 (2000) e11. https://doi.org/10.1557/S1092578300000119.
[23] S.J. Pearton, E.A. Douglas, R.J. Shul, F. Ren, Plasma etching of wide bandgap and ultrawide bandgap semiconductors, Journal of Vacuum Science & Technology A: Vacuum, Surfaces, and Films 38 (2020) 020802. https://doi.org/10.1116/1.5131343.
[24] P.-M. Coulon, G. Kusch, R.W. Martin, P.A. Shields, Deep UV Emission from Highly Ordered AlGaN/AlN Core–Shell Nanorods, ACS Appl. Mater. Interfaces 10 (2018) 33441–33449. https://doi.org/10.1021/acsami.8b10605.
[25] P.-M. Coulon, G. Kusch, P. Fletcher, P. Chausse, R. Martin, P. Shields, Hybrid Top-Down/Bottom-Up Fabrication of a Highly Uniform and Organized Faceted AlN Nanorod Scaffold, Materials 11 (2018) 1140. https://doi.org/10.3390/ma11071140.
[26] L. Jaloustre, V. Ackermann, S.S.D. Mello, S. Labau, C. Petit-Etienne, E. Pargon, Preferential crystal orientation etching of GaN nanopillars in Cl2 plasma, Materials Science in Semiconductor Processing 165 (2023) 107654. https://doi.org/10.1016/j.mssp.2023.107654.
[27] A.M. Efremov, G.-H. Kim, J.-G. Kim, C.-I. Kim, Self-consistent global model for inductively coupled Cl2 plasma: Comparison with experimental data and application for the etch process analysis, Thin Solid Films 515 (2007) 5395–5402. https://doi.org/10.1016/j.tsf.2007.01.027.
[28] C. Cardinaud, M.-C. Peignon, P.-Y. Tessier, Plasma etching: principles, mechanisms, application to micro- and nano-technologies, Applied Surface Science 164 (2000) 72–83. https://doi.org/10.1016/S0169-4332(00)00328-7.
[29] M. Brihoum, G. Cunge, M. Darnon, D. Gahan, O. Joubert, N.St.J. Braithwaite, Ion flux and ion distribution function measurements in synchronously pulsed inductively coupled plasmas, Journal of Vacuum Science & Technology A: Vacuum, Surfaces, and Films 31 (2013) 020604. https://doi.org/10.1116/1.4790364.
[30] L. Jaloustre, S.S.D. Mello, S. Labau, C. Petit-Etienne, E. Pargon, Faceting mechanisms of GaN nanopillar under KOH wet etching, Materials Science in Semiconductor Processing 173 (2024) 108095. https://doi.org/10.1016/j.mssp.2023.108095.
[31] M. Fouchier, E. Pargon, Atomic force microscopy study of photoresist sidewall smoothing and line edge roughness transfer during gate patterning, J. Micro/Nanolith. MEMS MOEMS 12 (2013) 041308. https://doi.org/10.1117/1.JMM.12.4.041308.
[32] D.L. Goldfarb, A.P. Mahorowala, G.M. Gallatin, K.E. Petrillo, K. Temple, M. Angelopoulos, S. Rasgon, H.H. Sawin, S.D. Allen, M.C. Lawson, R.W. Kwong, Effect of thin-film imaging on line edge roughness transfer to underlayers during etch processes, Journal of Vacuum Science & Technology B: Microelectronics and Nanometer Structures Processing, Measurement, and Phenomena 22 (2004) 647–653. https://doi.org/10.1116/1.1667513.
[33] C. Lee, D.B. Graves, M.A. Lieberman, Role of etch products in polysilicon etching in a high-density chlorine discharge, Plasma Chem Plasma Process 16 (1996) 99–120. https://doi.org/10.1007/BF01465219.
[34] T.L. Cottrell, The strengths of chemical bonds, Butterworths Scientific, 1954.
[35] B.D. Darwent, National Standard Reference Data Series, National Bureau of Standards, J. Chem. Educ. Wash. Dc (1965) 502.
[36] H.S. Kim, G.Y. Yeom, J.W. Lee, T.I. Kim, Characteristics of inductively coupled Cl2/BCl3 plasmas during GaN etching, Journal of Vacuum Science & Technology A: Vacuum, Surfaces, and Films 17 (1999) 2214–2219. https://doi.org/10.1116/1.581749.
[37] O. Luere, E. Pargon, L. Vallier, B. Pelissier, O. Joubert, Etch mechanisms of silicon gate structures patterned in SF6/CH2F2/Ar inductively coupled plasmas, Journal of Vacuum Science & Technology B, Nanotechnology and Microelectronics: Materials, Processing, Measurement, and Phenomena 29 (2011) 011028. https://doi.org/10.1116/1.3522656.
[38] H. Hübner, Calculations on Deposition and Redeposition in Plasma Etch Processes, J. Electrochem. Soc. 139 (1992) 3302–3309. https://doi.org/10.1149/1.2069072.
[39] P.-M. Coulon, P. Feng, T. Wang, P. Shields, Impact of Inductively Coupled Plasma Etching Conditions on the Formation of Semi-Polar (11-22) and Non-Polar (11-20) GaN Nanorods, Nanomaterials 10 (2020) 2562. https://doi.org/10.3390/nano10122562.
[40] N. Okada, K. Nojima, N. Ishibashi, K. Nagatoshi, N. Itagaki, R. Inomoto, S. Motoyama, T. Kobayashi, K. Tadatomo, Formation of distinctive structures of GaN by inductively-coupled-plasma and reactive ion etching under optimized chemical etching conditions, AIP Advances 7 (2017) 065111. https://doi.org/10.1063/1.4986766.
[41] B. Leung, M.-C. Tsai, G. Balakrishnan, C. Li, S.R. Brueck, J.J. Figiel, P. Lu, G.T. Wang, Highly Anisotropic Crystallographic Etching for Fabrication of High-Aspect Ratio GaN Nanostructures., Sandia National Lab.(SNL-NM), Albuquerque, NM (United States), 2016.
[42] J. He, M. Feng, Y. Zhong, J. Wang, R. Zhou, H. Gao, Y. Zhou, Q. Sun, J. Liu, Y. Huang, S. Zhang, H. Wang, M. Ikeda, H. Yang, On-wafer fabrication of cavity mirrors for InGaN-based laser diode grown on Si, Sci Rep 8 (2018) 7922. https://doi.org/10.1038/s41598-018-26305-8.

[43] W. Guo, J. Xie, C. Akouala, S. Mita, A. Rice, J. Tweedie, I. Bryan, R. Collazo, Z. Sitar, Comparative study of etching high crystalline quality AlN and GaN, Journal of Crystal Growth 366 (2013) 20–25. https://doi.org/10.1016/j.jcrysgro.2012.12.141.
[44] J.R. Mileham, S.J. Pearton, C.R. Abernathy, J.D. MacKenzie, R.J. Shul, S.P. Kilcoyne, Patterning of AlN, InN, and GaN in KOH-based solutions, Journal of Vacuum Science & Technology A: Vacuum, Surfaces, and Films 14 (1996) 836–839. https://doi.org/10.1116/1.580399.
[45] J.R. Mileham, S.J. Pearton, C.R. Abernathy, J.D. MacKenzie, R.J. Shul, S.P. Kilcoyne, Wet chemical etching of AlN, Applied Physics Letters 67 (1995) 1119–1121. https://doi.org/10.1063/1.114980.
[46] D. Li, M. Sumiya, S. Fuke, D. Yang, D. Que, Y. Suzuki, Y. Fukuda, Selective etching of GaN polar surface in potassium hydroxide solution studied by x-ray photoelectron spectroscopy, Journal of Applied Physics 90 (2001) 4219–4223. https://doi.org/10.1063/1.1402966.
[47] W. Guo, R. Kirste, I. Bryan, Z. Bryan, L. Hussey, P. Reddy, J. Tweedie, R. Collazo, Z. Sitar, KOH based selective wet chemical etching of AlN, AlxGa1−xN, and GaN crystals: A way towards substrate removal in deep ultraviolet-light emitting diode, Applied Physics Letters 106 (2015) 082110. https://doi.org/10.1063/1.4913705.
[48] Y.-Y. Lai, S.-C. Hsu, H.-S. Chang, Y.S. Wu, C.-H. Chen, L.-Y. Chen, Y.-J. Cheng, The study of wet etching on GaN surface by potassium hydroxide solution, Research on Chemical Intermediates 43 (2017) 3563–3572. https://doi.org/10.1007/s11164-016-2430-1.
[49] B.A. Kazanowska, K.R. Sapkota, P. Lu, A.A. Talin, E. Bussmann, T. Ohta, B.P. Gunning, K.S. Jones, G.T. Wang, Fabrication and field emission properties of vertical, tapered GaN nanowires etched via phosphoric acid, Nanotechnology 33 (2022) 035301. https://doi.org/10.1088/1361-6528/ac2981.